19th Brazilian Congress of Thermal Sciences and Engineering
November 6th–10th, 2022, Bento Gonçalves - RS - Brazil

ENCIT2022-0551
HIGH-RESOLUTION WRF-LES SIMULATIONS OF A DIURNAL CYCLE WITH A NOCTURNAL JET FROM A GRAVITY CURRENT OVER COMPLEX TERRAIN

William C. Radünz
Centre of Dynamics and Fluids, Escola Politécnica, University of São Paulo
williamradunz@gmail.com

Pedro Peixoto
Institute of Mathematics and Statistics, Department of Applied Mathematics, University of São Paulo
ppeixoto@usp.br

Bruno S. Carmo
Department of Mechanical Engineering, Escola Politécnica, University of São Paulo
bruno.carmo@usp.br

Franciano Puhales
Otávio C. Acevedo
Department of Physics, Federal University of Santa Maria
franciano.puhales@ufsm.br, otavio@ufsm.br

Alejandro Gutiérrez
Instituto de Mecánica de los Fluidos e Ingeniería Ambiental, Universidad de la República
aguti@fing.edu.uy

Adriane P. Petry
Department of Mechanical Engineering, Federal University of Rio Grande do Sul
adrianep@mecanica.ufrgs.br

Yoshiaki Sakagami
Department of Health and Service, Federal Institute of Santa Catarina, Florianópolis, Brazil
yoshi@ifsc.edu.br

Júlio César Passos
Department of Mechanical Engineering, Federal University of Santa Catarina
julio.passos@lepten.ufsc.br

Abstract. *We perform multiscale simulations using the Advanced-Research Weather Research and Forecasting (WRF-ARW) of a full diurnal cycle that includes the passage of a cold and stably-stratified gravity current close to midnight at the Morrinhos wind farm, in Northeast Brazil, a location with complex topography. Met mast observations are used to evaluate the modeling skill for each computational domain. In general, turbulence-related variables such as the friction velocity and the sensible heat flux were better represented in the LES domains. However, the modeling error for variables such as wind speed and direction were usually smaller for the coarser mesoscale domains, despite the topographic flattening. On the other hand, the LES domains simulated flow features absent in coarser domains, such as the lee waves produced by the nocturnal jet. Therefore, more sensitivity studies are necessary to tap into the full potential of multiscale simulations using LES.*

Keywords: *WRF-LES, wind energy, complex terrain, nocturnal jet, gravity current*

1. INTRODUCTION

Numerical weather prediction (NWP) models serve a wide range of applications that includes extreme event forecasting, pollutant dispersion, agriculture and wind energy. For the latter, NWP models can be used either to forecast winds and energy production at a specific site or to assess the spatial variability of wind resources across a certain region (Sanz Rodrigo *et al.*, 2017). One of the most commonly-known models of this kind is the *Weather Research and Forecasting* (WRF) model (Skamarock, 2008). It is a prognostic model that solves the compressible Euler equations in three-dimensional space and time, therefore being able to forecast four-dimensional variables, such as wind speed, temperature, humidity, cloud cover, and rain, amongst others, across a certain regional area. Many physical processes are parameterized, such as the turbulent transport by planetary boundary-layer (PBL) and surface-layer (SL) parameterization schemes. This regional portion of the globe that comprises the computational domain lies within the atmospheric scales of motion known as the mesoscale, thus the reason WRF is considered a "mesoscale model".

The atmospheric mesoscale refers to processes that typically occur over horizontal distances between a few to approximately 700 km, which lies between the larger synoptic scale (>700 km) and the smaller microscale (<3 km) (Stull, 2015). In the last decade, NWP models have been progressively used with higher spatial resolution, moving from a regional modeling resolution of 1–3 km (mesoscale) towards below 100 m (microscale) (Haupt *et al.*, 2019). Since PBL schemes were devised for the mesoscale, when an NWP model runs on the microscale the PBL scheme is usually switched-off and large-eddy simulation (LES) capabilities are switched-on (Mirocha *et al.*, 2017). This means the model has "multiscale modeling" capabilities. To bridge the mesoscale and the microscale with a single modeling framework, several nested computational domains are employed with increasing levels of horizontal resolution and decreasing area (Sanz Rodrigo *et al.*, 2017). They can communicate via lateral boundary conditions, and thus solutions from parent domains are mapped onto the child domain's lateral surfaces. Domains running at the mesoscale tend to use PBL parameterizations, whereas those in the microscale tend to use LES. Noteworthy, applications in complex terrain are especially demanding of higher resolution to improve the representation of topographic effects (Fernández-González *et al.*, 2018).

Several scientific problems arose in this trend of increasingly-higher modeling resolution (Haupt *et al.*, 2019). The main one refers to the range of scales known as the *terra incognita* (Wyngaard, 2004), which lies between the mesoscale and the microscale. Some authors reported that the *terra incognita* lies in the range of scales between 100 m to the PBL depth (Rai *et al.*, 2019). When PBL schemes are used within the *terra incognita*, such as when the horizontal grid resolution is smaller than the PBL depth, noise in simulated variables or numerical artifacts, such as horizontal convective rolls, can appear (Haupt *et al.*, 2019). Haupt *et al.* (2019) evaluated *terra incognita* issues in flat terrain and complex terrain, and stated that artifacts did occur in flat terrain, whereas mountain waves were properly simulated in complex terrain without artifacts. They suggested the topographic forcing played a role in mitigating the *terra incognita* issues in complex terrain.

Another important scientific problem is the proper simulation of winds around and within wind farms (Veers *et al.*, 2019), and those located in complex terrain can be especially difficult (Finnigan *et al.*, 2020). Some previous investigations were based on mast measurements and production data from a complex-terrain wind farm in Northeast Brazil, known as "Morrinhos" (Radünz *et al.*, 2020, 2021, 2022). Those studies revealed that the spatial variability of wind resources over complex terrain is enhanced in stable conditions (Radünz *et al.*, 2020), because winds are more prone to low-level topographic blocking and steering (on the windward face) and acceleration in the lee. Daytime convection and turbulence generate better mixing in the wind, which leads to smaller spatial variability in resources. This contrast between daytime and nighttime stability conditions was, in part, responsible for rather strange performance differences between two rows of turbines: during the day, upstream turbines would perform slightly better than those downstream. Conversely, during the nighttime, downstream turbines would perform better than those upstream (Radünz *et al.*, 2021). It remained unclear why the performance was much better after midnight, and not before midnight. Recently, high-resolution simulations with the WRF model revealed that in the period between December 25th to 31st 2018, a gravity current with cold, stable and fast-moving winds flows from the coast and reaches Morrinhos close to midnight, producing a nocturnal jet and a deeper layer of stable air (Radünz *et al.*, 2022). The deeper stable layer produces strong gravity-driven acceleration between the lee of the plateaus and the downstream valley, which is commonly referred to as "downslope winds". In (Radünz *et al.*, 2022), the WRF model employed traditional PBL parameterization schemes at 333 m horizontal resolution, thus well within the *terra incognita*.

The present investigation moves beyond Radünz *et al.* (2022) and crosses the *terra incognita* to perform high-resolution multiscale simulations in the microscale (∼100 m) using WRF's LES capability. A full diurnal cycle with the passage of a gravity current close to midnight at the Morrinhos wind farm, in Northeast Brazil, and the interaction of the nocturnal jet with the topography, which sometimes produces mountain lee waves, is challenging modeling-wise and a state-of-the-art scientific problem. The main goal is to evaluate how the model simulates wind and turbulence across scales (from mesoscale to microscale) using (i) validation with observations from a meteorological mast, which includes high-frequency measurements of a sonic anemometer to characterize turbulence, and (ii) identifying turbulent motions and potential numerical artifacts. In this study, we will focus solely on the simulation of the wind conditions and the

validation against observations from a meteorological mast.

2. METHODOLOGY

2.1 Site description

Figure 1 illustrates the geographical location of the Morrinhos wind farm, in the countryside of the state of Bahia, in Brazil. The nested computational domains, which will be described later on, were drawn as the white concentric squares. It is about 360 km inland from the coast in an ecosystem known as the "sertão". The prevailing eastern southeastern (ESE) winds are produced by the trade winds. Morrinhos is a cluster of six wind farms, each composed of 15 wind turbines. This study is focused on one of these, which is called the Campo Formoso I (CF1) wind farm.

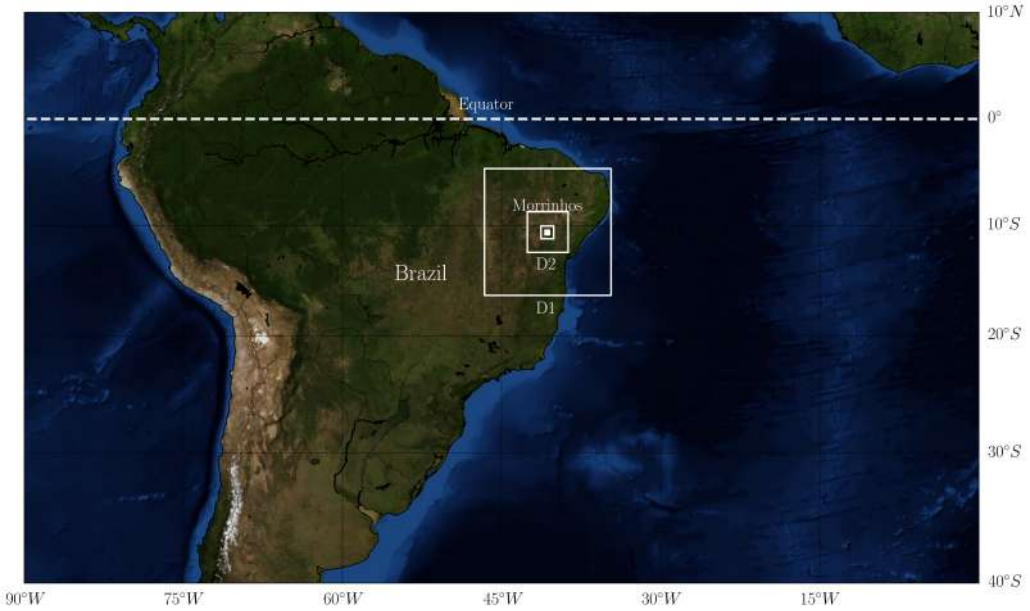

Figure 1. Geographical location of the Morrinhos wind farm site, in Northeast Brazil, and the representation of nested computational domains as white concentric squares.

Figure 2 represents the digital elevation model based on the *Shuttle Radar Topography Mission* (SRTM) Jarvis *et al.* (2008) data with a horizontal resolution of 90 m. The location of wind turbines and the meteorological mast are overlayed on the elevation map. A white line marks a vertical transect that was probed to assess the interplay between winds and topography. It is roughly aligned in the prevailing wind direction. The landscape is composed of chains of small plateaus with a downstream valley. Elevation variations of about 100–300 m in short horizontal distances are commonplace, and thus the "complex terrain" attribute is suitable for this site.

The meteorological mast is located immediately south of the last wind turbine. Owing to the prevailing ESE wind direction, measurements are rarely disturbed by turbines. Although the site can be generally characterized as "complex terrain", the winds blowing at the mast tend to be less disturbed by the interaction with the topography in comparison to those in the downstream valley, where flow separation and lee-wave activity can take place.

2.2 Observations and computed variables

Meteorological mast observations between the December 25th to 27th 2018 period and sensor equipment are summarized in Tab. 1. These include a cup anemometer, a wind vane, a thermohygrometer, and an ultrasonic three-component anemometer. The subindex in variables denotes the height above ground level (agl) at which the measurement was made. For instance, the wind speed measured at 78 m agl is expressed as "U_{78}". Most observations are gathered at 1 Hz and averaged over 10 minutes. The exception is the high-frequency measurements of wind speed components and sonic temperature, at 20 Hz.

Two parameters are computed based on the high-frequency observations of the sonic anemometer, which are the friction velocity ($u_\star$) and the sensible heat flux (H_s)

$$u_\star = \left[(\overline{u'w'})^2 + (\overline{v'w'})^2\right]^{1/4}, \tag{1}$$

$$H_s = \rho c_p \overline{\theta'_v w'}, \tag{2}$$

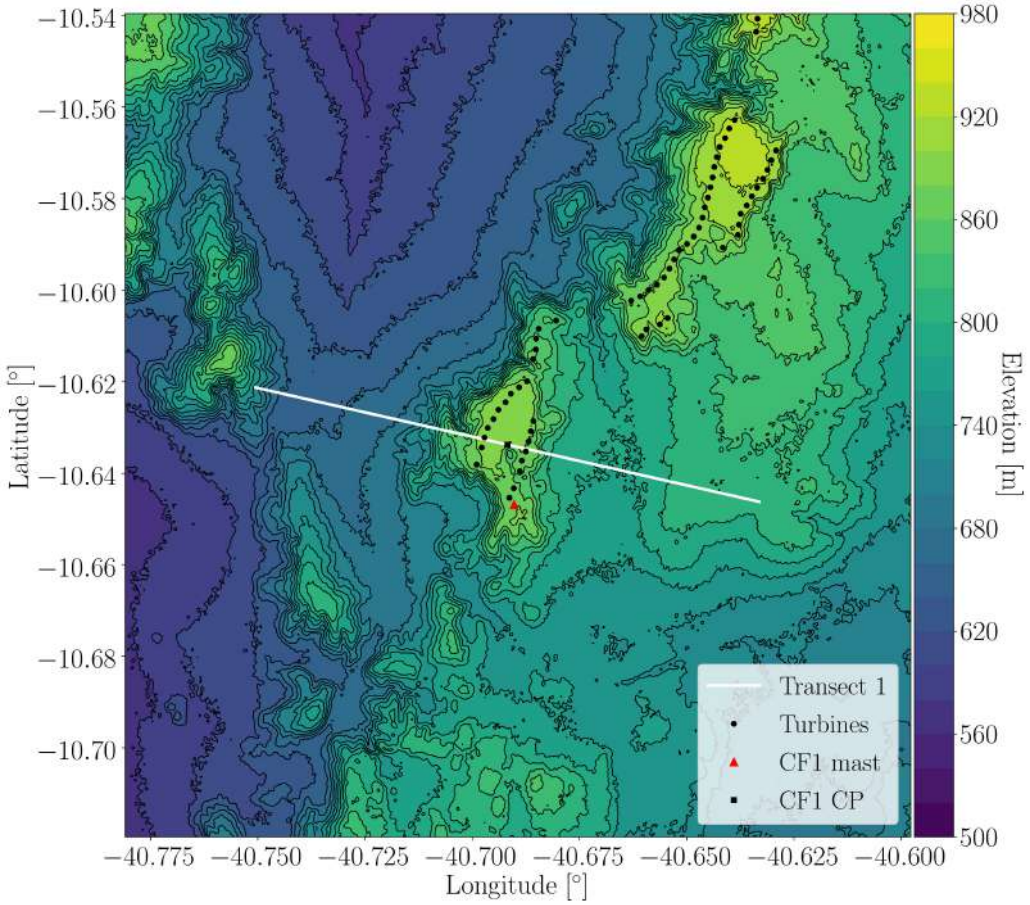

Figure 2. Digital elevation model for the CF1 wind farm area, where wind turbine locations are shown as black dots, the meteorological mast equipped with multiple sensors is the red triangle and the white line is the vertical transect used for analyses.

Table 1. Suite of sensors from the meteorological mast and measured variables employed in the study.

Variable	Sensor	Temporal resolution
Wind speed (U_{78})	cup anemometer	10 min (avg.)
Wind direction (WD_{76})	wind vane	10 min (avg.)
Air temperature (T_{68})	thermohygrometer	10 min (avg.)
Wind speed components (u, v, w)	3D sonic anemometer	1/20 s
Sonic temperature (T_{10})	3D sonic anemometer	1/20 s

where $\overline{u'w'}$ and $\overline{v'w'}$ are turbulent momentum fluxes, $\overline{\theta'_v w'}$ the kinematic heat flux, ρ the air density and c_p the specific heat of air. Hourly averages of the turbulent fluxes ($\overline{u'w'}$, $\overline{v'w'}$ e $\overline{\theta'_v w'}$) were processed with the open-source software EddyPro v. 6.2.2 (LI-COR Biosciences, 2019). We employed the eddy-covariance technique using *planar fit* and *linear detrending* methods, which are available in the software. The variables $u_\star$ and H_s, given by Eq. (1) and (2), respectively, are important to characterize the representation of turbulent processes both in the observations and numerical simulations.

2.3 Numerical simulations

The multiscale simulations were performed with the WRF model version 3.8.1 (Skamarock, 2008) using five telescoping nested domains with horizontal resolutions ranging from 8100 m (D1) to 100 m (D5), shown in Fig. 3. These were previously shown as the white rectangles in Fig. 1. The model solves the compressible Euler equations for the three spatial dimensions and time. Several processes are included via parameterization schemes, such as cloud formation physics, radiation, and the exchange of momentum, heat and moisture with the land surface.

Initial and lateral boundary conditions (LBC) for the outermost domain are provided by the ERA5 global reanalysis (Hersbach *et al.*, 2020), with a horizontal resolution of about 27.75 km and hourly temporal resolution. Input variables from the global reanalysis model are available at several vertical pressure levels and at the surface. The outermost domain

uses LBCs of the "specified" type. Hence, the variables for the first layer of cells from the computational domain are prescribed for the forcing reanalysis. Adjacent to these, a "relaxation layer" of cells can be nudged to the forcing reanalysis to prevent a drift from the driving synoptic-scale weather in the mesoscale model. This technique is known as "grid nudging" (Vincent and Hahmann, 2015). The wind speed, potential temperature and water vapor mixing ratio variables are nudged toward the large-scale forcing of the reanalysis, in grid-node space and for all wavelengths, at the relaxation zone of the outermost domain only.

Parent and child domains communicate via LBCs in a one-way-coupling approach. The nests use an LBC of the "specified" type based on the solutions of their parent domains, which are mapped onto the lateral surfaces. There is no relaxation zone, nor grid nudging, for the nested domains. Thus, the higher-resolution fields of child domains do not influence parent domains (no two-way coupling). This was intentionally set up to evaluate how each domain represents wind and turbulence separately. The domains are sequentially initialized to enable enough time for proper spin-up in parent domains. Thus, child domains are only initialized once the parent domain has spun up. The D1 domain initializes at 2018-12-25 09:00, D2 6 hours later at 2018-12-25 15:00, D3 6 hours later at 2018-12-25 21:00, and D4 and D5 are initiated jointly at 2018-12-26 09:00. Then, a full diurnal cycle is run until 2018-12-27 09:00.

The main differences in the modeling setup are summarized in Tab. 2. Turbulent processes in the atmospheric column can be either approached using planetary boundary-layer (PBL) schemes or large-eddy simulation (LES). LES is suitable for very-high-resolution grids running close to the microscale ($\sim$100 m), as the assumptions of PBL schemes are violated in this range. Thus, for domains near the microscale, PBL schemes are switched off and LES mode is enabled. The outermost domains (D1–D3) employ the YSU planetary boundary-layer (PBL) parameterization scheme (Song-You Hong and Dudhia, 2006), whereas for the two innermost domains (D4–D5) we switch off the PBL scheme and activate the large-eddy simulation (LES) mode. The Deardorff subgrid scale model was used for the LES (Deardorff, 1980). The Monin-Obukhov surface-layer (SL) scheme was employed for all domains. Cumulus parameterization via the Kain–Fritsch (Kain, 2004; Kain and Fritsch, 1990) scheme was activated only for the outermost domain.

Land-use and topography classes were based on the Noah-modified 21-category IGBP-MODIS. We employed the RRTM Mlawer *et al.* (1997) and the Dudhia Lacis and Hansen (1974); Stephens (1978) schemes for longwave and shortwave radiation processes. We also used the WRF Single-Moment 5-class cloud microphysics scheme (WSM5) Hong *et al.* (2004) and the Noah land surface model Chen and Dudhia (2001).

Table 2. Main differences in modeling setup for all domains.

	SL scheme	PBL scheme	LES	Topography	e_{we}	e_{sn}	e_{vert}
D1 (8100 m)	MO	YSU	off	GMTED2010 (1 km)	163	163	61
D2 (2700 m)	MO	YSU	off	GMTED2010 (1 km)	157	157	61
D3 (900 m)	MO	YSU	off	GMTED2010 (1 km)	148	148	61
D4 (300 m)	MO	–	on	SRTM (90 m)	154	154	61
D5 (100 m)	MO	–	on	SRTM (90 m)	202	202	61

Two datasets were used for digital terrain elevation. For D1–D3, WRF's native Global Multi-resolution Terrain Elevation Data 2010 (GMTED2010) (Danielson and Gesch, 2011), with a horizontal resolution of about 1 km, was employed. For D4–D5, the higher-resolution data (90 m) from the *Shuttle Radar Topography Mission* (SRTM) (Jarvis *et al.*, 2008) seemed the better choice for proper topographic representation. The terrain elevation for each domain is shown in Fig. 3. Table 2 also shows the number of grid nodes for the computational domains in the west-east (e_{we}), south-north (e_{sn}) and vertical (e_{vert}) directions. In the vertical direction, the nodes are not uniformly distributed to provide higher resolution near the ground. Thus, we specified 20 nodes below 1 km agl, and the remaining 41 progressively become coarser as they approach the top of the computational domain ($\sim$20 km or 50 hPa pressure level). For example, D1 spans roughly 1300 km (8100 m $\times$ 163 nodes) in the horizontal directions. The innermost domain has a larger number of nodes because it was intentionally extended to provide a larger fetch, necessary for the turbulence spin-up.

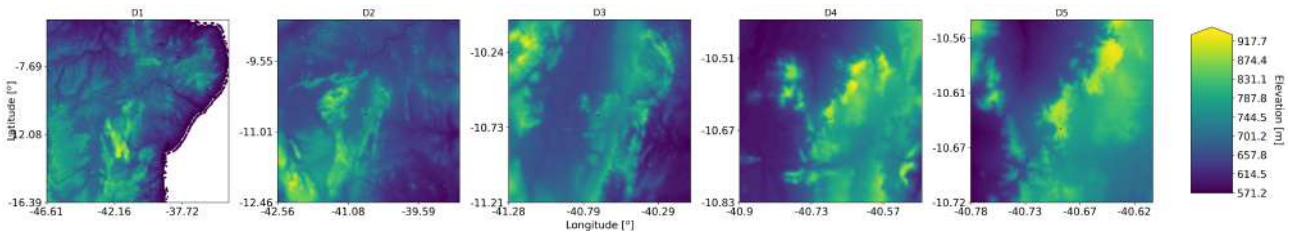

Figure 3. Terrain elevation represented for each computational domain. The color bar refers to the last domain only.

3. RESULTS

3.1 Validation with met mast

Figure 4 displays the time series of wind speed (U_{78}), direction (WD_{76}), potential temperature (θ_{68}), shear (α_{78-20}), friction velocity ($u_\star$) and sensible heat flux (H_s) for the simulated diurnal cycle. The wind shear between 20 and 78 m agl was calculated as $\alpha_{78-20} = ln(U_{78}/U_{20})/ln(78/20)$. Results were linearly interpolated to the met mast coordinate for all domains. Daytime fluctuations in all variables for the LES domains illustrate the representation of turbulent convection, absent in coarser domains. Shorty after 23:00, wind speeds increase abruptly and temperatures drop at the arrival of a cold-air gravity current, reported in a previous investigation (Radünz *et al.*, 2022). All domains represent this process reasonably well except for the D1 domain, which shows a delayed and smoothed response. This diurnal cycle is characterized by weaker and more turbulent winds during the daytime, which is seen by the higher $u_\star$ and H_s, closely related to turbulence. The H_s is maximum close to 13:00, the time of largest sun heat, but the air is hottest later on at 15:00. H_s progressively decreases after 13:00 and becomes small and negative close to 18:00, whereby the ground cools down faster than the overlying air, thus absorbing heat from the latter. This is the onset of the nocturnal stable layer and the decay of turbulence. $u_\star$ abruptly increases by the time the gravity current advects past the site because of the stronger and more turbulent winds, despite the stable stratification.

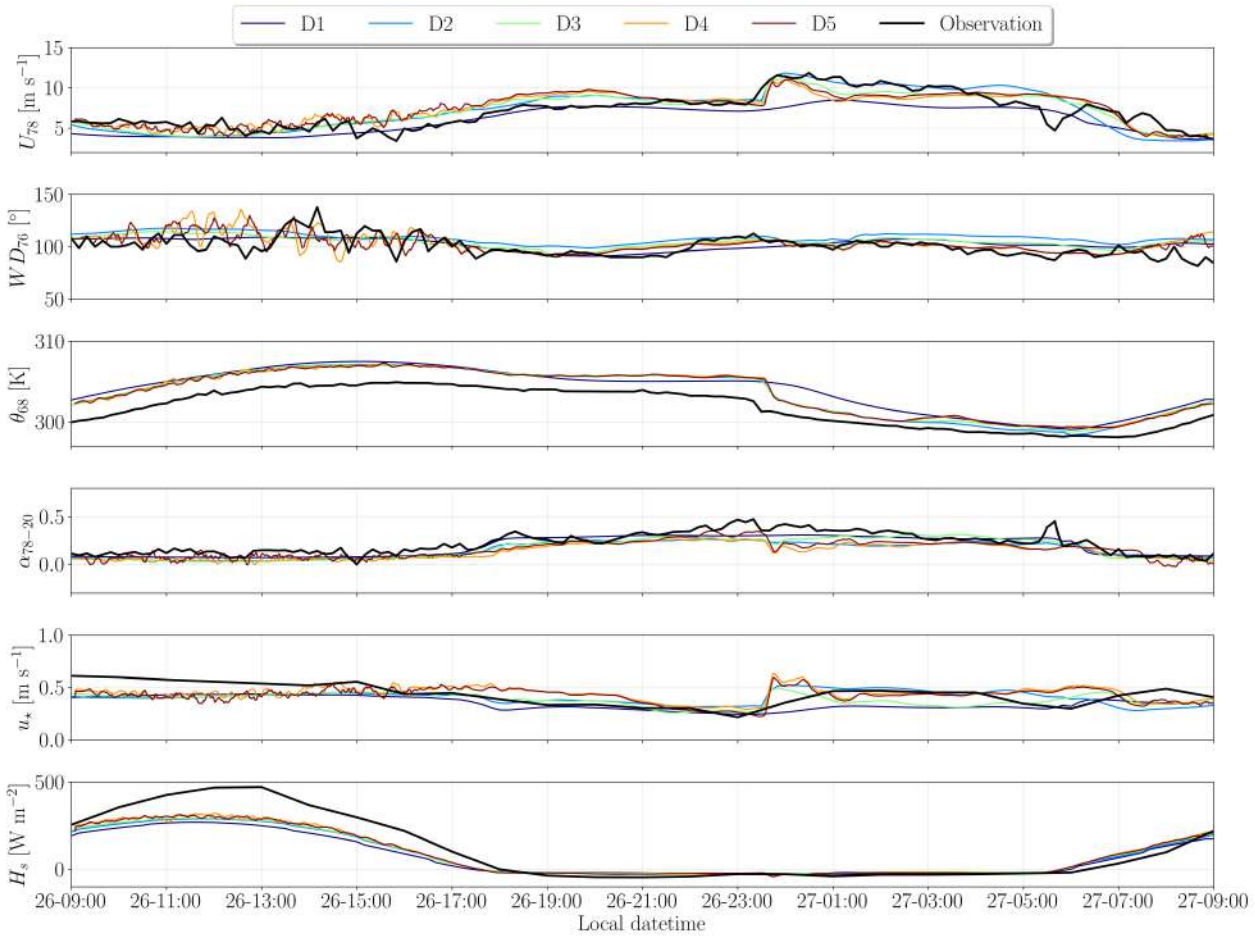

Figure 4. Time series of simulated wind speed (U_{78}), direction (WD_{76}), potential temperature (θ_{68}), shear (α_{78-20}), friction velocity ($u_\star$) and sensible heat flux (H_s) were linearly interpolated to the mast coordinates for all domains to enable a comparison with the observations.

Two error metrics were employed for validation. The first is the mean absolute error (MAE), defined as $MAE = \sum_{i=1}^{n} |e_i|/n$, where i stands for the time index, n the sample size and $|e_i|$ is the absolute error between simulation and observation. The second is the BIAS, defined as $BIAS = \sum_{i=1}^{n} e_i/n$, where the error now retains its sign. Tables 3–5 summarize the MAE and BIAS error metrics for all variables and domains in comparison with the observations. We segregated the metrics between daytime (10:00 to 17:00, Tab. 3), early nighttime (19:00 to 23:00, Tab. 4) and late nighttime (00:00 to 06:00, Tab. 5) to evaluate modeling skills in different wind and turbulence conditions, as these are sensitive to

the diurnal cycle. We purposely removed the morning, evening transition and gravity-current arrival periods.

Table 3. MAE/BIAS metrics for selected variables related to the daytime period between 26-10:00 to 17:00.

Domain	U_{78} [m s^{-1}]	WD_{76} [°]	α_{78-20}	$u_\star$ [m s^{-1}]	H_s [W m^{-2}]
D1	1.05/-0.87	8/0	0.05/-0.05	0.1/-0.1	157.19/-157.19
D2	1.09/-0.16	11/6	0.08/-0.07	0.1/-0.1	134.06/-134.06
D3	1.08/-0.09	10/3	0.08/-0.08	0.1/-0.1	130.03/-130.03
D4	1.09/0.49	13/4	0.08/-0.08	0.09/-0.06	119.47/-119.47
D5	1.24/0.55	13/3	0.08/-0.05	0.11/-0.09	121.99/-121.99

Table 4. MAE/BIAS metrics for selected variables related to the early nighttime period between 26-19:00 to 23:00.

Domain	U_{78} [m s^{-1}]	WD_{76} [°]	α_{78-20}	$u_\star$ [m s^{-1}]	H_s [W m^{-2}]
D1	0.51/-0.45	4/-2	0.05/-0.02	0.02/-0.02	20.14/20.14
D2	0.77/0.75	8/8	0.07/-0.07	0.04/0.04	17.01/17.01
D3	0.67/0.53	5/4	0.06/-0.06	0.03/0.01	18.92/18.92
D4	0.97/0.97	5/2	0.08/-0.08	0.07/0.07	14.78/14.78
D5	0.99/0.95	5/2	0.05/-0.05	0.06/0.05	16.04/16.04

Table 5. MAE/BIAS metrics for selected variables related to the late nighttime period between 27-00:00 to 06:00.

Domain	U_{78} [m s^{-1}]	WD_{76} [°]	α_{78-20}	$u_\star$ [m s^{-1}]	H_s [W m^{-2}]
D1	1.98/-1.72	6/5	0.05/-0.03	0.11/-0.11	7.8/7.8
D2	0.94/0.75	11/11	0.09/-0.09	0.06/0.05	10.36/10.17
D3	1.11/-0.07	6/6	0.06/-0.03	0.09/-0.05	13.23/13.2
D4	1.52/-0.44	3/1	0.12/-0.12	0.07/0.04	9.95/9.62
D5	1.33/-0.2	3/2	0.1/-0.1	0.07/0.03	9.39/9.33

During the daytime (Tab. 3), the D4–D5 LES domains produced smaller MAE/BIAS for the $u_\star$ and H_s variables. For U_{78}, D5 led to the worst metrics and D2–D3 to the best BIAS. Domain D1 better represented the WD_{76} and α_{78-20} variables. For the early nighttime (Tab. 2), the D4–D5 LES domains produced the best (H_s) and worst (U_{78}) metrics for some variables. Surprisingly, the best metrics for U_{78}, WD_{76} and α_{78-20} were for the coarsest domain (D1). After midnight (Tab. 3), the D4–D5 LES domains presented good metrics for the WD_{76}, $u_\star$ (with D2) and H_s (with D1); for α_{78-20}, it led to the worst metrics. Domain D3 had the best metrics for U_{78} (with D2, low MAE; and D5, low BIAS). Therefore, turbulent-fluxes-related variables ($u_\star$ and H_s) were better represented in the LES domains. That was not the case for other variables, except for some situations.

Since the LES domains resolve the larger scales of turbulent motion, being more realistic than the coarser domains in this sense, the better skill in forecasting $u_\star$ and H_s is reasonable. As for the other variables, two factors may hint at the underlying causes for modeling skill. The first is that higher resolution and topographic detail would ideally improve the microscale flow field and, thus, the forecast. The second is that PBL schemes can be superior to the LES, or vice-versa, depending on the domain and the hour of the day. It could be argued that owing to the decay of turbulence in the nocturnal stable-layer, the LES domains are too coarse to resolve the larger scales during the nighttime. As such, PBL schemes outperforming the LES is reasonable. However, applying the same rationale for the daytime, whereby convection produces turbulent motion of larger scales, the LES could potentially outperform the PBL schemes. However, the LES does not outperform the PBL schemes during the daytime, and we speculate no further. A more detailed sensitivity study would be necessary to fully address this issue.

3.2 Maps of variables at fixed heights

Figure 5 depicts the potential temperature at a fixed height of 10 m agl for all domains and three different periods of the diurnal cycle. The thermal contrast between land and sea is evident for D1, where land is hotter during the daytime. However, during the nighttime the cold air near the coastline propagates inland as a gravity current, having already past the site by 00:00. This air is colder than that overlying the sea because of the nocturnal cooling over land. At 10:00, the colder air (yellow) overlying the São Francisco river around the hotter surroundings (red) is visible. Daytime convective turbulence, responsible for the fluctuations in Fig. 4, is visible for the LES domains. The smoother contours during the nighttime reveal the inhibition of turbulence.

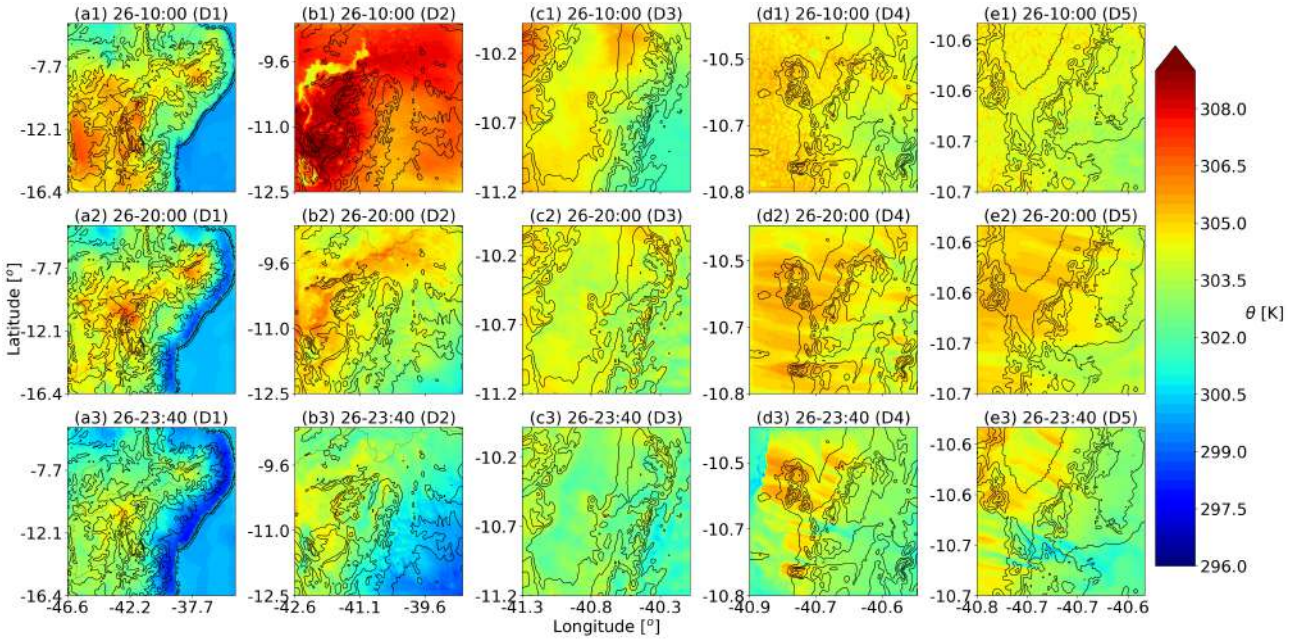

Figure 5. Some snapshots of potential temperature at a fixed height of 10 m agl for each domain.

Figure 6 shows snapshots of wind speed (x-component) at a fixed height of 100 m agl for the innermost domain. Similar to Fig. 5d-e1, daytime convection produces wind gusts with variable, both positive and negative, wind speed components. Turbulent structures are artificially smoother near the boundaries because of the boundary conditions and become finer as they flow over the domain. Hence the importance of a domain large enough to allow for the spin-up of turbulence. At night (Fig. 6b), the wind speed field is smoothly distributed and with maximum values occurring near the downstream valley (dark blue colors). The 26-23:40 snapshot captures the fast-moving front of the gravity current, having just past the mast (Fig. 6c). At 27-06:00 (Fig. 6d), two features are evident: first, that turbulence is produced in the downstream valley; second, there is a considerable wind speed gradient over the plateaus because of the downslope winds.

3.3 Vertical transects of variables

Figures 7 and 8 show snapshots of vertical transects of potential temperature and wind speed (x component), respectively. Results for different domains are represented across lines. The cross-section of the terrain is colored grey and the approximate mast location is represented as a black dot.

The spatial variability of potential temperature is helpful to understand atmospheric stability and wind patterns. At noon, the vertical variability of potential temperature is small owing to convection (Figs. 7a1–e1). The daytime convective structures are well-represented in the LES domains (Figs. 7d1–e1) but absent in the non-LES ones (Figs. 7a1–c1), as they should. As these turbulent wind gusts are transported by the mean wind, measurements at the met mast display strong fluctuations in wind speed during the daytime (Figs. 8d1–e1 and 4). At night, the vertical stratification in potential temperature, with colder air near the ground, characterizes the nocturnal stable layer (Figs. 7a2–e2). The flow becomes less perturbed as turbulent motion is suppressed.

The gravity current front is captured by the 23:40 snapshot (Figs. 7b3–e3 and 8b3–e3), except for the outermost domain, which has a delayed response (Figs. 7a3 and 8a3). The gravity current features colder and stronger winds as advects past the site. The progressive increase in resolution enables resolving flow features that are mostly smoothed out in the coarser domains (Figs. 7b3–c3).

At 06:00, the large potential temperature gradients at higher levels depict a deeper stable-layer of air (Figs. 7a4–e4) in comparison to the early nighttime period (Figs. 7a2–e2). The coarse D1 and D2 domains flattened the topographic features and inhibited the appearance of mountain lee waves, clearly visible in Figs. 7d4–e4. These waves can appear whenever winds of a stable layer of air are disturbed/blocked by topography, such as hills and mountains (Queney, 1948). Notably, winds near the lee accelerate considerably owing to this interaction, which was shown to be the main cause underlying the better performance of downstream turbines relative to upstream turbines close to the met mast (Radünz *et al.*, 2022). Thus, the spatial variability of winds is completely misrepresented for domains D1 and D2. The downslope winds in the lee only appear subsequently to the D3 domain.

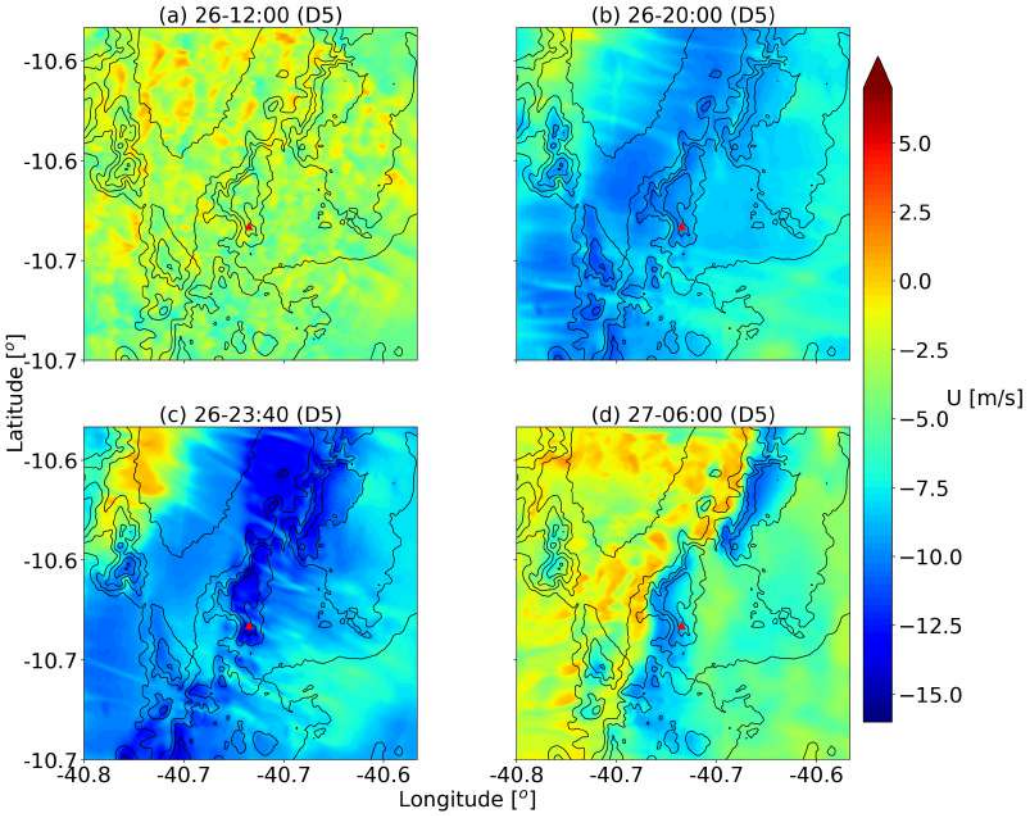

Figure 6. Some snapshots of the x-component of the wind speed at a fixed height of 100 m agl for the innermost domain.

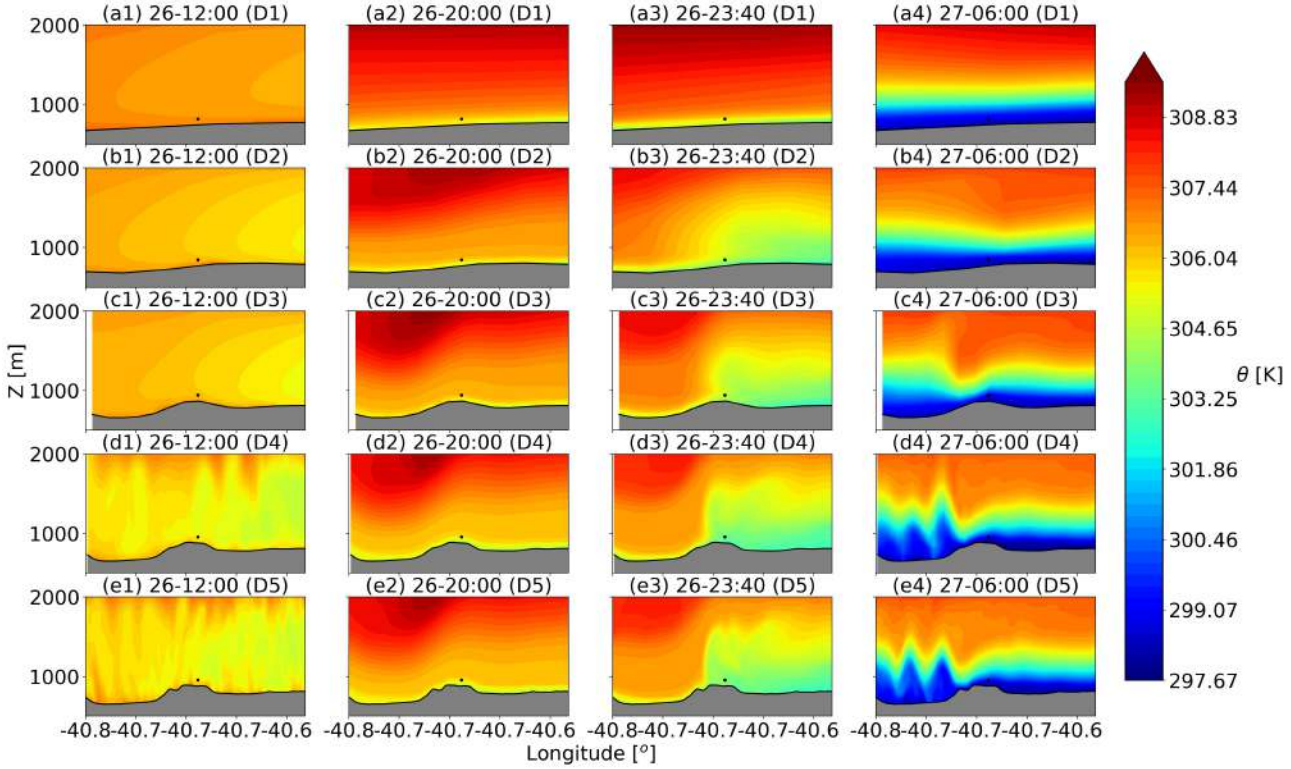

Figure 7. Potential temperature snapshots at 26-12:00, 26-20:00, 26-23:40 and 27-06:00 are represented in each column, for the vertical transects illustrate the enhanced topographic detail across domains, represented in each line. The arrival of the gravity current's front appears at 26-23:40.

4. CONCLUSIONS

In this paper, multiscale simulations using the WRF model were employed to simulate a full diurnal cycle with the passage of a gravity current front close to midnight. Five nested domains downscaled winds from the ERA5 reanalysis

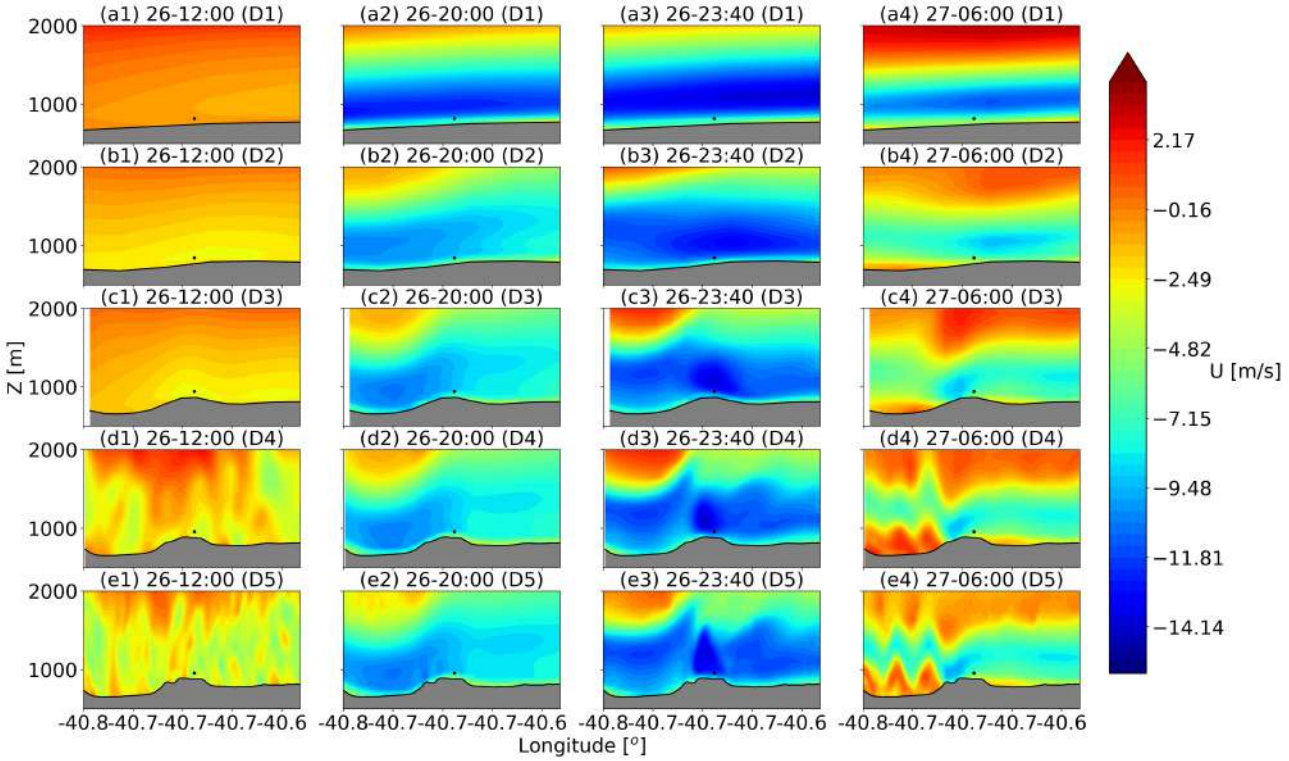

Figure 8. Same as Fig. 7, but for the x-component of wind speed.

at the synoptic-scale toward the mesoscale (low resolution) and the microscale (high resolution). Domains running in the mesoscale employed PBL parameterization schemes, whereas those running in the microscale disabled PBL schemes and enabled the LES mode. Observations from a met mast from the Morrinhos wind farm, located over complex terrain, were used for validation.

Since the nested domains were one-way coupled, child domains did not influence the results from parent domains. This enabled a fair assessment of the skill amongst domains. Since winds, turbulence, models and parameterizations are sensitive to the diurnal cycle, the MAE and BIAS metrics for selected variables were segregated based on the following periods: daytime (10:00–17:00), early nighttime (19:00–23:00), and late nighttime (00:00–06:00). The domains running with LES (D4 and D5) displayed an improved representation of turbulence-related variables, such as the $u_\star$ and H_s, almost at all times. However, the improved representation of turbulence did not lead to an improved skill for wind speed and shear, for example. Wins speed was best represented by the domains D3 (daytime), D1 (early nighttime) and D3/D2/D5 (late nighttime). Thus, the LES domains displayed a good skill for wind direction and wind speed only in the late nighttime period.

The advection of the gravity current across the site close to 23:40 was well represented by domains D2–D5, and delayed for domain D1. Differences in flow features were clear as the horizontal resolution increased between domains. Importantly, the topography was nearly flattened-out for domains D1–D2. Mountain lee waves were only properly represented for domains D4 and D5. The daytime fine-scale turbulent convection was simulated by the LES domains and absent in the coarser domains, as they should be. Turbulence produced by the breakage of lee waves within the valley is also represented by the LES before sunrise.

Therefore, the high-resolution LES domains improved the skill for turbulence-related variables, but not so much for other variables. In some cases, the coarsest domain produced the best results for a specific variable, despite the flattening of the topography. This trend may be partly attributed to the fact that the met mast was located in an area of lesser terrain and flow complexity. In the downstream valley, where intricate processes such as lee waves take place, the coarser domains were unable to properly represent the flow features. If the meteorological mast was installed there, results would likely be superior for LES. Further model sensitivity investigations are necessary to understand and improve the high-resolution simulations. Future research could improve turbulence characterization by using spectral analysis.

5. ACKNOWLEDGEMENTS

We are thankful to *CGN Brasil Energia e Participações* for providing valuable field observations, and to *ClusterUY* (*Universidad de La República*) for the computational resources for the simulations. W. C. Radünz would like to thank FAPESP for financial support. B. S. Carmo thanks the CNPq for financial support in the form of a productivity grant,

number 314221/2021-2. P. Peixoto would like to thank FAPESP, grant number 2021/06176-0, for financial support.

6. REFERENCES

Chen, F. and Dudhia, J., 2001. "Coupling an advanced land-surface/ hydrology model with the Penn State/ NCAR MM5 modeling system. Part I: Model description and implementation." *Monthly Weather Review*, Vol. 129, No. 1, pp. 569–585. doi:https://doi.org/10.1175/1520-0493(2001)129<0569:CAALSH>2.0.CO;2.

Danielson, J.J. and Gesch, D.B., 2011. "Global Multi-resolution Terrain Elevation Data 2010 (GMTED2010)". Technical report, U.S. Department of the Interior, U.S. Geological Survey.

Deardorff, J.W., 1980. "Stratocumulus-capped mixed layers derived from a three-dimensional model". *Boundary-Layer Meteorology*, Vol. 18, No. 4, pp. 495–527. ISSN 0006-8314. doi:10.1007/BF00119502.

Fernández-González, S., Martín, M.L., García-Ortega, E., Merino, A., Lorenzana, J., Sánchez, J.L., Valero, F. and Rodrigo, J.S., 2018. "Sensitivity analysis of the WRF model: Wind-resource assessment for complex terrain". *Journal of Applied Meteorology and Climatology*, Vol. 57, No. 3, pp. 733–753. ISSN 15588432. doi:10.1175/JAMC-D-17-0121.1.

Finnigan, J., Ayotte, K., Harman, I., Katul, G., Oldroyd, H., Patton, E., Poggi, D., Ross, A. and Taylor, P., 2020. "Boundary-Layer Flow Over Complex Topography". *Boundary-Layer Meteorology*, Vol. 177, No. 2-3, pp. 247–313. ISSN 15731472. doi:10.1007/s10546-020-00564-3. URL `https://doi.org/10.1007/s10546-020-00564-3`.

Haupt, S.E., Kosovic, B., Shaw, W., Berg, L.K., Churchfield, M., Cline, J., Draxl, C., Ennis, B., Koo, E., Kotamarthi, R., Mazzaro, L., Mirocha, J., Moriarty, P., Muñoz-Esparza, D., Quon, E., Rai, R.K., Robinson, M. and Sever, G., 2019. "On Bridging A Modeling Scale Gap: Mesoscale to Microscale Coupling for Wind Energy". *Bulletin of the American Meteorological Society*, Vol. 100, No. 12, pp. 2533–2550. ISSN 0003-0007. doi:10.1175/bams-d-18-0033.1.

Hersbach, H., Bell, B., Berrisford, P., Hirahara, S., Horányi, A., Muñoz-Sabater, J., Nicolas, J., Peubey, C., Radu, R., Schepers, D., Simmons, A., Soci, C., Abdalla, S., Abellan, X., Balsamo, G., Bechtold, P., Biavati, G., Bidlot, J., Bonavita, M., De Chiara, G., Dahlgren, P., Dee, D., Diamantakis, M., Dragani, R., Flemming, J., Forbes, R., Fuentes, M., Geer, A., Haimberger, L., Healy, S., Hogan, R.J., Hólm, E., Janisková, M., Keeley, S., Laloyaux, P., Lopez, P., Lupu, C., Radnoti, G., de Rosnay, P., Rozum, I., Vamborg, F., Villaume, S. and Thépaut, J.N., 2020. "The ERA5 global reanalysis". *Quarterly Journal of the Royal Meteorological Society*, Vol. 146, No. 730, pp. 1999–2049. ISSN 1477870X. doi:10.1002/qj.3803.

Hong, S.Y., Dudhia, J. and Chen, S.H., 2004. "A Revised Approach to Ice Microphysical Processes for the Bulk Parameterization of Clouds and Precipitation". *Monthly Weather Review*, Vol. 132, No. 1, pp. 103–120. doi:https://doi.org/10.1175/1520-0493(2004)132<0103:ARATIM>2.0.CO;2.

Jarvis, A., Reuter, H.I., Nelson, A. and Guevara, E., 2008. "Hole-filled SRTM for the globe Version 4". Technical report, CGIAR-CSI. doi:available from the CGIAR-CSI SRTM 90m Database (http://srtm.csi.cgiar.org).

Kain, J.S., 2004. "The Kain-Fritsch convective parameterization: An update". *Journal of Applied Meteorology and Climatology*, Vol. 43, No. 1, pp. 170–181. doi:https://doi.org/10.1175/1520-0450(2004)043<0170:TKCPAU>2.0.CO;2.

Kain, J.S. and Fritsch, J.M., 1990. "A one-dimensional entraining/detraining plume model and its application in convective parameterization". *Journal of Applied Meteorology and Climatology*, Vol. 47, No. 23, pp. 2784–2802.

Lacis, A.A. and Hansen, J.E., 1974. "A parameterization for the absorption of solar radiation in the earth's atmosphere." *Journal of Atmospheric Sciences*, Vol. 31, No. 1, pp. 118–133.

LI-COR Biosciences, 2019. "EddyPro Instruction Manual". URL `licor.com/documents/1ium2zmwm6hl36yz9bu4`.

Mirocha, J.D., Churchfield, M.J., Muñoz-Esparza, D., Rai, R.K., Feng, Y., Kosović, B., Haupt, S.E., Brown, B., Ennis, B.L., Draxl, C., Sanz Rodrigo, J., Shaw, W.J., Berg, L.K., Moriarty, P.J., Linn, R.R., Kotamarthi, V.R., Balakrishnan, R., Cline, J.W., Robinson, M.C. and Ananthan, S., 2017. "Large-Eddy Simulation Sensitivities to Variations of Configuration and Forcing Parameters in Canonical Boundary-Layer Flows for Wind Energy Applications". *Wind Energy Science Discussions*. ISSN 2366-7621. doi:10.5194/wes-2017-33.

Mlawer, E.J., Taubman, S.J., Brown, P.D., Iacono, M.J. and Clough, S.A., 1997. "Radiative transfer for inhomogeneous atmosphere: RRTM, a validated correlated-k model for the long-wave." *Journal of Geophysical Research*, Vol. 102, No. d14, pp. 16663–16682. doi:https://doi.org/10.1029/97JD00237.

Queney, P., 1948. "The Problem of Air Flow Over Mountains: A Summary of Theoretical Studies". *Bulletin of the American Meteorological Society*, Vol. 29, No. 1, pp. 16–26. ISSN 0003-0007. doi:10.1175/1520-0477-29.1.16.

Radünz, W.C., de Almeida, E., Gutiérrez, A., Acevedo, O.C., Sakagami, Y., Petry, A.P. and Passos, J.C., 2022. "Nocturnal jets over wind farms in complex terrain". *Applied Energy*, Vol. 314, p. 118959. ISSN 03062619. doi:10.1016/j.apenergy.2022.118959.

Radünz, W.C., Sakagami, Y., Haas, R., Petry, A.P., Passos, J.C., Miqueletti, M. and Dias, E., 2020. "The variability of wind resources in complex terrain and its relationship with atmospheric stability". *Energy Conversion and Management*, Vol. 222, p. 113249. ISSN 01968904. doi:10.1016/j.enconman.2020.113249.

Radünz, W.C., Sakagami, Y., Haas, R., Petry, A.P., Passos, J.C., Miqueletti, M. and Dias, E., 2021. "Influence of

atmospheric stability on wind farm performance in complex terrain". *Applied Energy*, Vol. 282, p. 116149. ISSN 03062619. doi:10.1016/j.apenergy.2020.116149.

Rai, R.K., Berg, L.K., Kosović, B., Haupt, S.E., Mirocha, J.D., Ennis, B.L. and Draxl, C., 2019. "Evaluation of the impact of horizontal grid spacing in terra incognita on coupled mesoscale-microscale simulations using the WRF framework". *Monthly Weather Review*, Vol. 147, No. 3, pp. 1007–1027. ISSN 15200493. doi:10.1175/MWR-D-18-0282.1.

Sanz Rodrigo, J., Chávez Arroyo, R.A., Moriarty, P., Churchfield, M., Kosović, B., Réthoré, P.E., Hansen, K.S., Hahmann, A., Mirocha, J.D. and Rife, D., 2017. "Mesoscale to microscale wind farm flow modeling and evaluation". *Wiley Interdisciplinary Reviews: Energy and Environment*, Vol. 6, No. 2, p. e214. ISSN 20418396. doi:10.1002/wene.214. URL `http://doi.wiley.com/10.1002/wene.214`.

Skamarock, W.C., 2008. "Description of the Advanced Research WRF Version 3 (No. NCAR/TN-475+STR)." Technical report, University Corporation for Atmospheric Research. doi:http://dx.doi.org/10.5065/D68S4MVH.

Song-You Hong, Y.N. and Dudhia, J., 2006. "A new vertical diffusion package with an explicit treatment of entrainment processes". *Monthly Weather Review*, Vol. 134, No. 9, p. 2318–2341. doi:https://doi.org/10.1175/MWR3199.1.

Stephens, G.L., 1978. "Radiation profiles in extended water clouds. Part II: Parameterization schemes". *Journal of Atmospheric Sciences*, Vol. 35, No. 1, pp. 2123–2132. ISSN 1520-0469. doi:https://doi.org/10.1175/1520-0469(1978)035<2123:RPIEWC>2.0.CO;2.

Stull, R., 2015. *Practical Meteorology - An Algebra-based Survey of Atmospheric Science*. University of British Columbia. ISBN 978-0-88865-176-1. doi:10.14288/1.0300441.

Veers, P., Dykes, K., Lantz, E., Barth, S., Bottasso, C.L., Carlson, O. and Clifton et al., A., 2019. "Grand challenges in the science of wind energy". *Science*, Vol. 366, No. 6464, p. eaau2027. ISSN 0036-8075. doi:10.1126/science.aau2027.

Vincent, C.L. and Hahmann, A.N., 2015. "The impact of grid and spectral nudging on the variance of the near-surface wind speed". *Journal of Applied Meteorology and Climatology*, Vol. 54, No. 5, pp. 1021–1038. ISSN 15588432. doi:10.1175/JAMC-D-14-0047.1.

Wyngaard, J.C., 2004. "Toward numerical modeling in the "Terra Incognita"". *Journal of the Atmospheric Sciences*, Vol. 61, No. 14, pp. 1816–1826. ISSN 00224928. doi:10.1175/1520-0469(2004)061<1816:TNMITT>2.0.CO;2.

7. RESPONSIBILITY NOTICE

The authors are solely responsible for the printed material included in this paper.